DOI: 10.13009/EUCASS2019-128

Lateral-Directional Aerodynamics of a Re-usable Re-entry Vehicle

Tamás Bykerk, Giuseppe Pezzella**, Dries Verstraete* and Antonio Viviani***
** University of Sydney, School of Aerospace, Mechanical and Mechatronic Engineering*
tamas.bykerk@sydney.edu.au; dries.verstraete@sydney.edu.au
*** University of Campania, Engineering Department*
giuseppe.pezzella@unicampania.it; antonio.viviani@unicampania.it

Abstract

Re-usable, unmanned flying test-beds are an efficient way to experimentally validate next generation high-speed re-entry technologies. During descent, the vehicle will be exposed to free-stream velocities ranging from hypersonic to low subsonic, which requires a careful choice of aeroshape. Mission success depends on the vehicle being stable during both low and high-speed phases of flight and it is key to understand stability and control authority for both conditions. In this framework, the paper focuses attention on the V-one research programme, a research collaboration between the University of Sydney and University of Campania, which aims to investigate the aerodynamics of a slender spatuled wing-body concept. The lateral-directional characteristics of the vehicle concept were analysed through wind tunnel and CFD. The vehicle was subjected to a range of angle of attack and sideslip, with asymmetric elevon and full moving ruddervator deflections up to 10 degrees. The force and moment coefficients were evaluated about a reference centre at 45% of the vehicle length. Low speed studies showed similar trends for stability between wind tunnel and CFD results. Control derivatives extracted from subsonic and hypersonic CFD simulations show sufficient control authority. However, in isolated cases with high angle of attack and sideslip results showed a tendency of flow separation on the fins at low speed and flap at high speed, reducing directional stability and control effectiveness.

1. Introduction

Over the last decades, advanced concepts of high-speed transportation vehicles were provided and investigated. These concepts have a great potential to increase vehicle performances such as cross-range and aerodynamic efficiency, thanks to innovative high-lift aeroshapes. Nonetheless, performing a test campaign (i.e., flight and Wind Tunnel, WT) represents the only and ultimate proof to demonstrate the technical feasibility of these new promising concepts. In this framework, the V-one project, carried out by University of Sydney and University of Campania within a joint research programme, intends to investigate, through both numerical and wind tunnel test activities, an innovative (unpowered) high speed glider, namely V-one, shown in Figure 1.

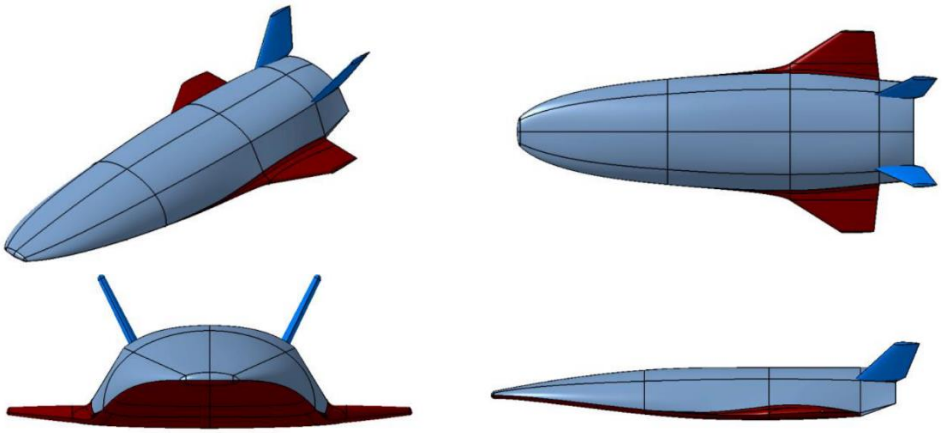

Figure 1: Views of the unpowered V-One vehicle concept.

DOI: 10.13009/EUCASS2019-128

As shown, the concept is a test-bed glider which features a relatively simple architecture which aims to embody all the features of an operational system. It consists of a low aspect ratio wing with two vertical stabilizer (butterfly configuration) and a spatuled fuselage on top of the wing with the forebody characterized by a rounded off two-dimensional leading edge. The combined elevator and aileron (elevon) is shown in purple in Figure 2 along with the complete moving fins (ruddervators) in green. The ruddervators have a pivot point located at 50% of the fin chord length.

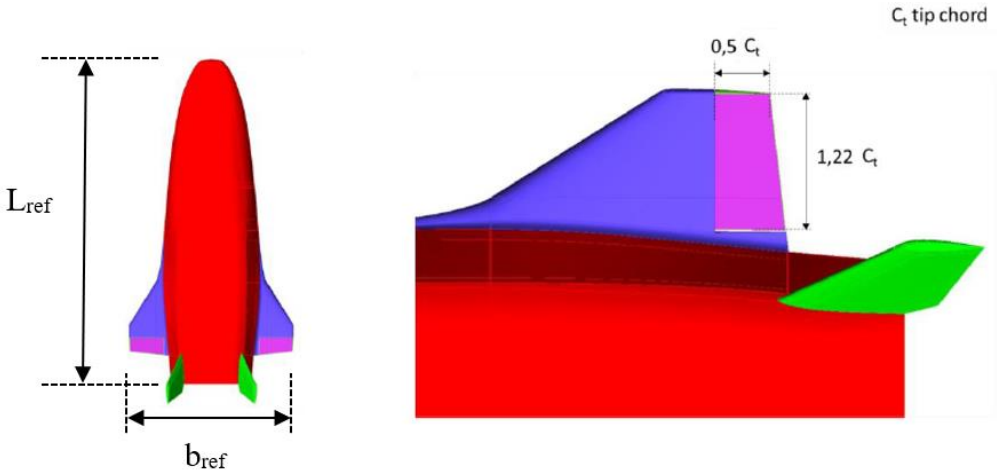

Figure 2: Elevon and ruddervator sizing.

This research programme aims to create the basis for a step-by-step increase of the readiness level of several enabling technologies suitable for high-speed hypersonic flight, such as aeroshape aerodynamics assessment. During a typical flight mission, the aircraft will encounter free-stream velocities ranging from hypersonic to low subsonic. This demands to careful choice concept aeroshape. For the mission to be successful, the vehicle aeroshape will need to be stable and manoeuvrable during both low and high-speed phases of flight.

In line with this long-term goal, current research programme objectives are to gain experience on aerodynamic performances and flying qualities (i.e., static stability in longitudinal and lateral-directional flight with aerosurfaces control authority) of this unconventional aeroshape, giving confidence that a full-scale concept could be a viable option to provide to research centres, space agencies or industries for their own high-speed research programmes.

Vehicle aerodynamics assessment was undertaken with both numerical (i.e., CFD) and experimental (i.e., WT) approaches. Low (subsonic) and high-speed (a design point Mach number of 7) conditions were investigated. In this framework, the paper aims to build on past research presented by the same authors in Ref. [1], which determined a MRC at 45% of the vehicle length was able to provide longitudinal and lateral-directional static stability. It also demonstrated the aircraft can be trimmed in pitch with the selected elevon size. Results presented here will focus on vehicle lateral-directional control effectiveness by testing ruddervator and asymmetric elevon deflections (i.e., ailerons) at various angles of attack (AoA) and sideslip (AoS). Subsonic CFD investigations are conducted for some of the cases and are performed under the same conditions as a WT test campaign to validate and compare numerical results. Starting from those investigations further changes could be operated on vehicle aeroshape, in the light of oncoming suggestions by new research targets and goals. CFD aerodynamic analyses were carried out at different attitudes and vehicle configurations (i.e. for different aerodynamic surfaces deflections). Then, an overview of the aerodynamic characteristics of the V-one concept is performed. with the goal to provide aerodynamic database (AEDB) for flight mechanics analyses. Indeed, it must be verified that concept aerodynamic control surfaces are able to provide lift at hypersonic to stay within the loads constraint during flight. Glider AEDB is being developed and set-up as a function of Mach number, angle of attack, sideslip, ruddervator and aileron deflections, according to the trajectory-based approach, by performing a large number of WT and CFD simulations.

2. Methodology

2.1 Low speed

The wind tunnel test campaign was completed in the 7 x 5 foot low-speed facility at the University of Sydney. The model was fabricated using an assembly of 3D printed pieces, which were then glued together and sanded for a smooth finish. The vehicle was scaled to a length of 0.662 metres, with a reference area of 0.129 m^2 and a span width of 0.33 m. Wind tunnel tests were conducted at 30 m/s and a Reynolds number of approximately $1.3x10^6$. Wind tunnel data

DOI: 10.13009/EUCASS2019-128

was taken using a six components load cell recessed in the body of the model to reduce interference. Images of the model in the tunnel are shown in Figure 3.

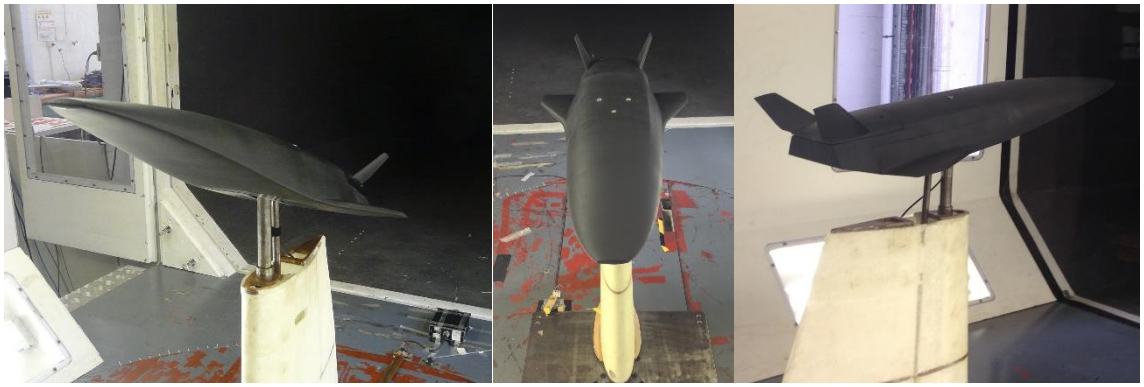

Figure 3: Views of the model in the 7 x 5 wind tunnel

The low speed CFD studies covered a range of AoA from -5 to 15 degrees at increments of 5 degrees. At each of these points, the aircraft was swept through an AoS range of -8 to 8 degrees, with steps of 1 degree. This was first completed for the clean configuration (no controls deflected) and was then repeated for asymmetric elevon deflections of 5 and 10 degrees and ruddervator settings of -5 and -10 degrees. Note that the ruddervator and elevons were deflected independently of each other. Wind tunnel tests were conducted for the clean configuration only.

The CFD component was run using ANSYS FLUENT® to compare with tunnel data and visualise flow features not able to be seen in the wind tunnel tests. The Reynolds Averaged Navier-Stokes (RANS) equations are integrated by means of the finite volume approach. The Reynolds number of the CFD has been set to match the wind tunnel tests to allow a fair comparison of data. The simulations were run using the steady state and the SST k-ω turbulence model. The mesh is comprised of unstructured elements with prism inflation layers for boundary layer discretization (Y^+=O(1) at wall). As shown in Figure 4, the grid features a body of influence surrounding the vehicle for mesh refinement. The domain extends approximately 15 chord lengths upstream and 25 downstream. To properly model the side slip condition, a full body mesh was required and comprised of approximately 15 million elements.

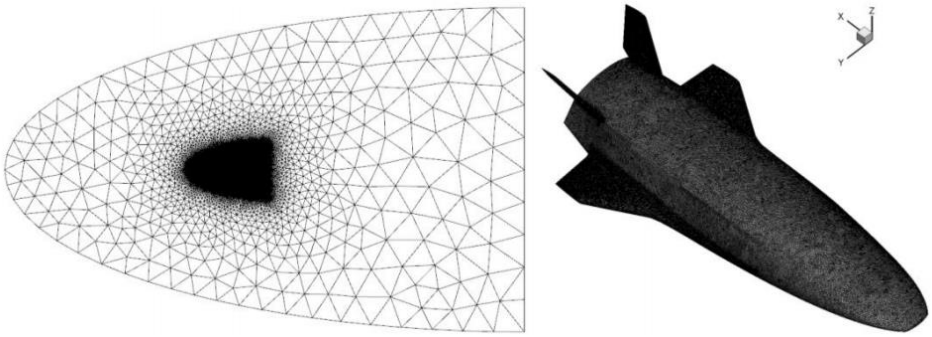

Figure 4: View of unstructured domain and vehicle mesh for low-speed analyses.

2.2 High speed

High-speed CFD simulation were carried-out with both multi-block structured and hybrid grids. An example of those meshes is provided in for the case of 10 degrees elevon deflection and is shown in Figure 5. The computational domain is tailored for the free-stream conditions of the selected flight points and vehicle attitude and configurations (different aerosurfaces deflections). Therefore, for each case, a new grid has been created to properly accommodate for the detached bow shock location. The baseline grid topology for this work consists of 51 blocks for an overall number of about 7 M cells (half body). Then, the grid is constructed to permit local refinement to improve numerical results. In particular, the mesh was initially generated algebraically and then adapted as the solution evolved (i.e., solution adaptive approach), aligning the grid with the bow shock and clustering points in the boundary layer, with the constraint condition of Y^+=O(1) at wall.

DOI: 10.13009/EUCASS2019-128

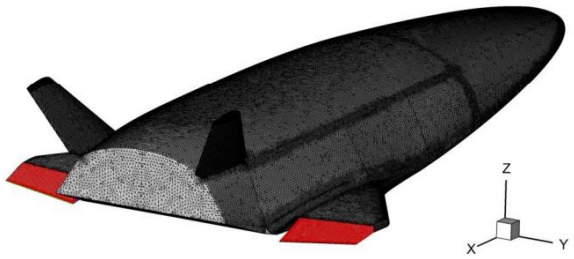

Figure 5: View of unstructured vehicle mesh for 10 deg elevon deflections.

Lateral-deflections numerical investigations requested grids with a number of about 16 M cells (full-body). High speed simulations are also performed using the steady state solver in ANSYS FLUENT® with SST k-ω turbulence model. The Flux Difference Splitting (FDS) second-order upwind scheme (least square cell based) has been used for the spatial reconstruction of convective terms, while for the diffusive fluxes a cell-centred scheme has been applied. An implicit scheme has been considered for time integration. The ideal gas model for air was assumed to remain valid as the aeroshape features a very slender configuration and will fly at rather low angle of attack (i.e., weak attached shock waves). A temperature-dependent formulation was considered for the specific heat at constant pressure c_p (i.e., thermally perfect gas) to accommodate the rather high flow energy [2]. The following polynomial formulation for the c_p was found using Eq.(1), where the flow temperature ranges from 100 K to 2000 K.

$$C_p = 5.71 \times 10^{-18}T^6 - 9.79 \times 10^{-14}T^5 + 5.22 \times 10^{-10}T^4 - 1.27 \times 10^{-6}T^3 + 1.46 \times 10^{-3}T^2 - 5.46 \times 10^{-1}T + 1.07 \times 10^3 \quad \textbf{(1)}$$

For T<100 K c_p=1039.59 [J/kg/K], while for T>2000 K c_p=1265.35 [J/kg/K]. Sutherland's relationship was assumed for the dynamic viscosity. As far as boundary conditions are concerned, the radiative cooled wall (ε=0.8) was assumed for all the flight conditions.

High-speed CFD investigations focused on vehicle attitude ranging from 0 to 20 deg AoA and sideslip angle from -2 to 2 deg. Then, effects of ailerons (asymmetric) deflections from -10 to 10 deg were explored together with AoS ranging from -8 to 8 deg. So far, ruddervators were set in clean configurations only to take into account for the build-up approach in the development of the vehicle AEDB. Next planned CFD simulations will focus on the ruddervators' contributions only to complete the contribution of each vehicle part on its aerodynamics.

2.3 Axis conventions and derivative evaluation

Aircraft aerodynamics are provided according to the ISO-1151 standard and is the convention usually adopted in flight mechanics. The side force coefficient (C_Y), rolling moment coefficient (C_l) and the yawing moment coefficient (C_n) are the parameters which determine the lateral-directional characteristics of the aircraft. These are all in the vehicle body reference frame (BRF), which is illustrated in Figure 6. Control deflections are also defined within the standard, with positive asymmetric elevon deflections are considered when the trailing edge (TE) on the left wing is down. Ruddervator deflections are positive when the trailing edge is deflected to the left.

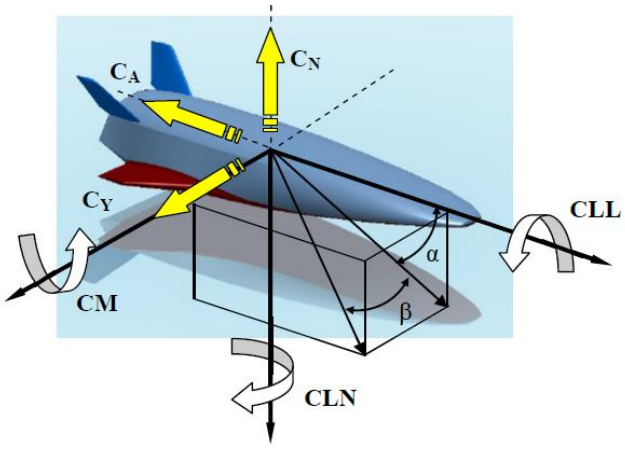

Figure 6: Vehicle BRF with aerodynamic force and moment coefficients.

DOI: 10.13009/EUCASS2019-128

Table 1 presents the derivatives for controls and lateral-directional aerodynamics for static stability. To evaluate the derivatives, expected ranges for typical aircraft from Roskam are also shown (in the form min/max limit) [3].

Table 1: Summary of lateral-directional stability criteria

Derivative	Description	Range	Derivative	Description	Range
$C_{Y\beta}$	Gradient of C_Y vs β	-2/-0.1	$C_{n\delta e}$	Gradient of C_n vs δ_e	-0.08/0.08
$C_{n\beta}$	Gradient of C_n vs β	0/0.4	$C_{l\delta r}$	Gradient of C_l vs δ_r	-0.04/0.04
$C_{l\beta}$	Gradient of C_l vs β	-0.4/0.1	$C_{n\delta r}$	Gradient of C_n vs δ_r	-0.15/0
$C_{l\delta e}$	Gradient of C_l vs δ_e	0/0.4	$C_{Y\delta r}$	Gradient of C_Y vs δ_r	0/0.5

3. Results and discussion

3.1 Low speed

Figure 7, Figure 8 and Figure 9 present results from rolling moment, yawing moment and side force respectively. For roll, positive derivatives at low AoA and indicate static instability due to sideslip. The trends observed match well with wind tunnel data, however wind tunnel tests indicate slightly increased stability. Comparisons between tunnel data for yaw and side force again show similar trends, but experimental data displays higher stability compared with CFD. For each of case the derivative results are within expected ranges.

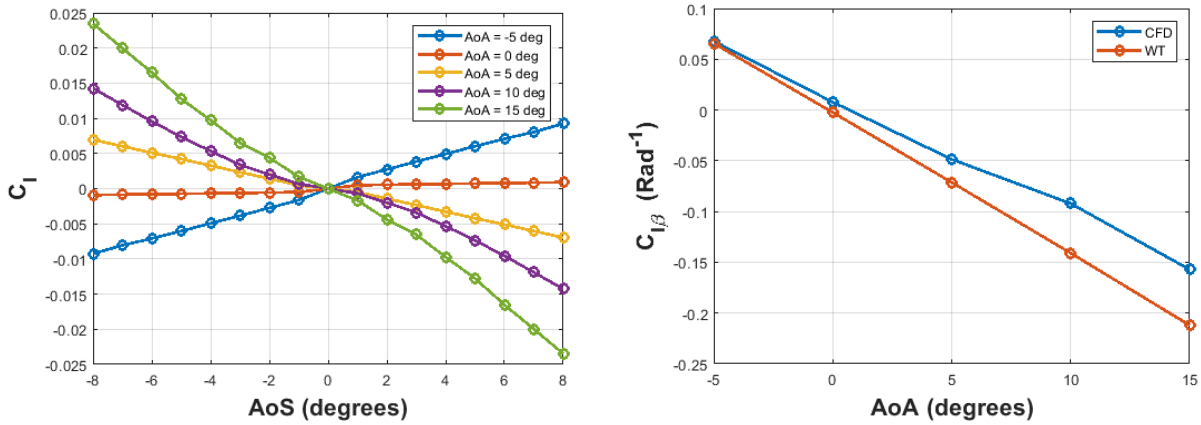

Figure 7: C_l vs AoS (left) and wind tunnel/CFD comparison for C_{l_β} derivative vs AoA

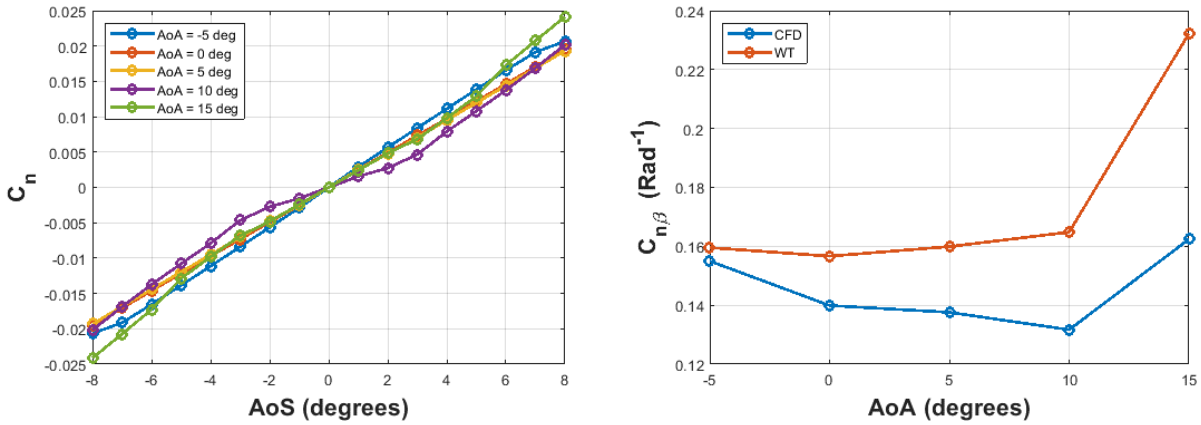

Figure 8: C_n vs AoS (left) and wind tunnel/CFD comparison for C_{n_β} derivative vs AoA

DOI: 10.13009/EUCASS2019-128

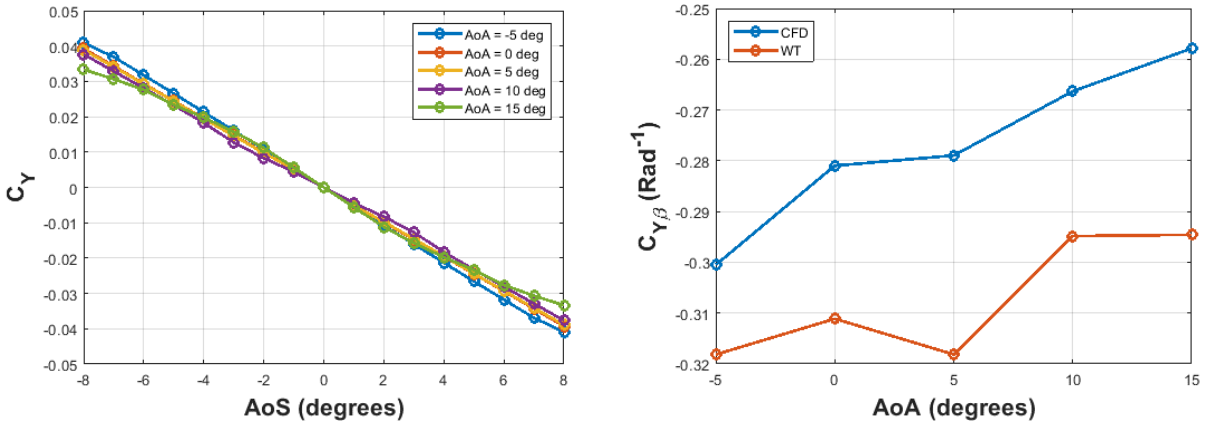

Figure 9: C_Y vs AoS (left) and wind tunnel/CFD comparison for C_{Y_β} derivative vs AoA

Figure 10 and Figure 11 show images of each fin with no control deflections at two different sideslip conditions for 0 degrees AoA. Surface flow visualisation and contours of pressure coefficient highlight the susceptibility of the left fin to flow separation at high AoS compared with the right hand side. This is due to both toe and cant angles, which create a locally higher AoA reducing the effectiveness of the vertical stabiliser at high AoS.

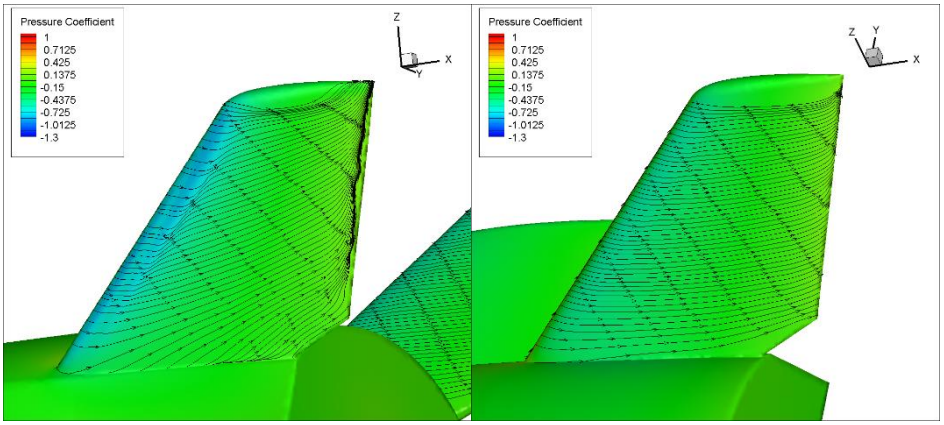

Figure 10: Leeward side of LHS fin 0 degrees AoA and 4 degrees AoS, (b) Leeward side of RHS fin 0 degrees AoA and 4 degrees AoS

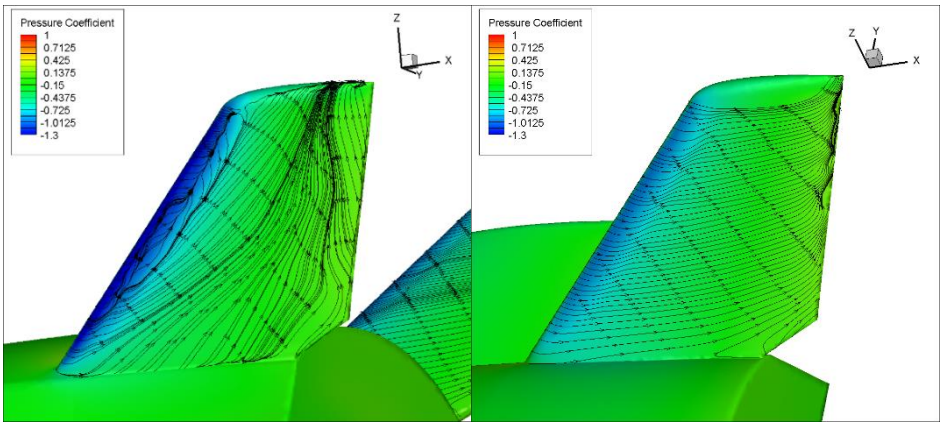

Figure 11: Leeward side of LHS fin 0 degrees AoA and 8 degrees AoS and (d) Leeward side of RHS fin 0 degrees AoA and 8 degrees AoS

Figure 12 and Figure 13 present the same AoS conditions for an AoA of 15 degrees. At low AoS, the flow on the left fin remains attached, with separation and cross flow observed on the right-hand side. At high AoS, the flow over the right fin shows increased flow separation, while the left fin appears to have minor separation combined with a region

DOI: 10.13009/EUCASS2019-128

of upflow caused by air coming off the rear portion of the fuselage. This is a potential cause of the observed reduction in sideforce coefficient with increasing AoA.

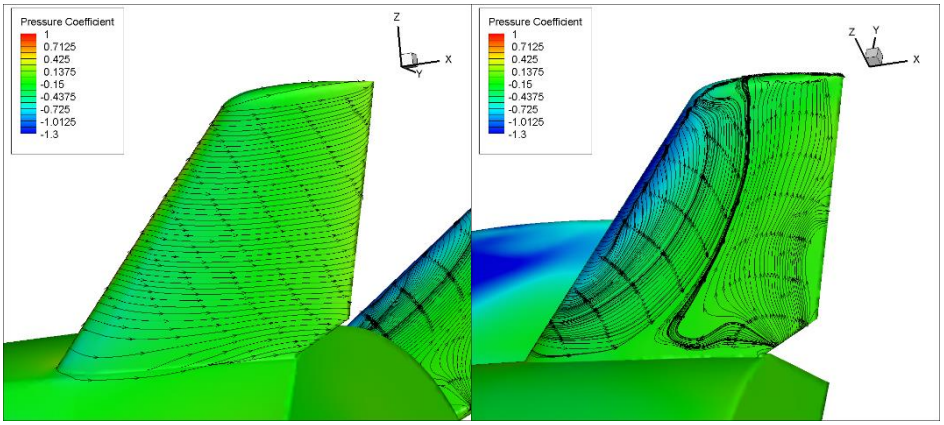

Figure 12: Leeward side of LHS fin 15 degrees AoA and 4 degrees AoS (left) and Leeward side of RHS fin 15 degrees AoA and 4 degrees AoS (right)

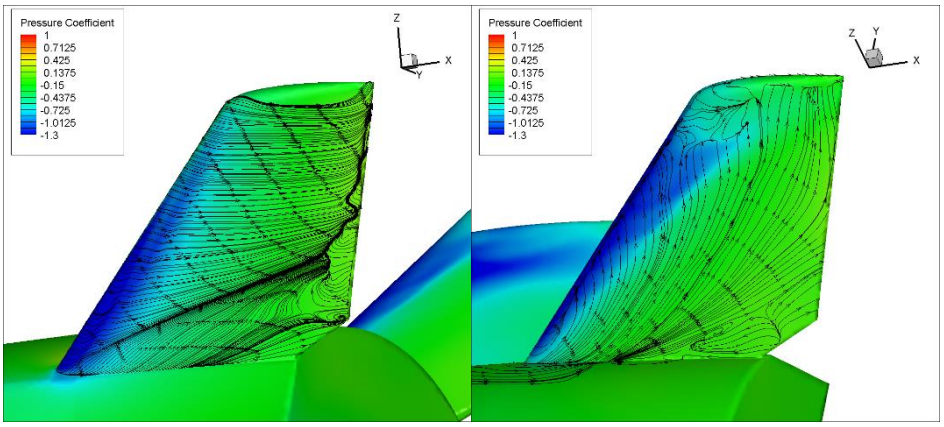

Figure 13: Leeward side of LHS fin 15 degrees AoA and 8 degrees AoS (left) and Leeward side of RHS fin 15 degrees AoA and 8 degrees AoS (right)

Figure 14 shows examples of staggered plots caused by asymmetric elevon deflections against rolling moment coefficient, while Figure 15 illustrates elevon effectiveness with increasing AoA. Positive elevon deflection is seen to increase the rolling moment coefficient as expected. Increased effectiveness is seen with increasing AoA.

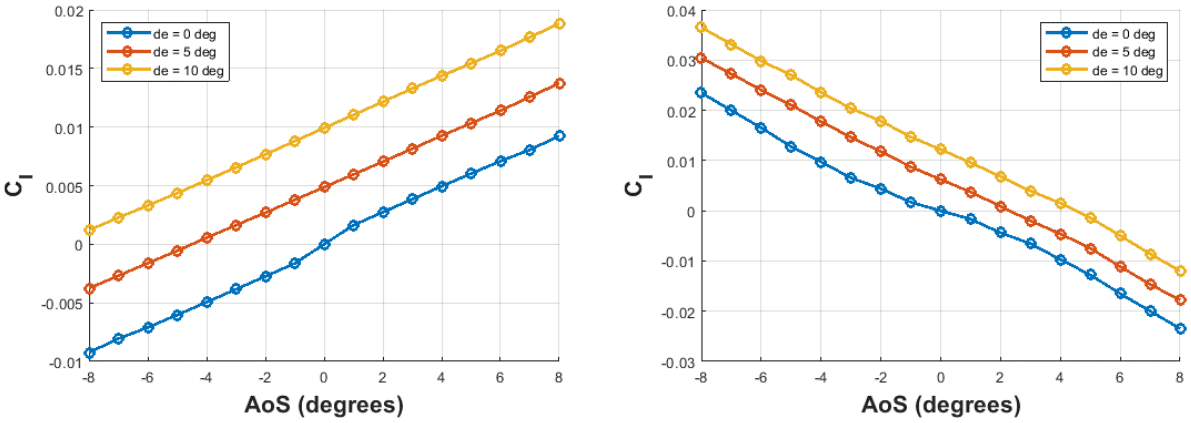

Figure 14: C_l vs AoS at -5 degrees AoA (left) and C_l vs AoS at 15 degrees AoA (right) for elevon deflection angles

DOI: 10.13009/EUCASS2019-128

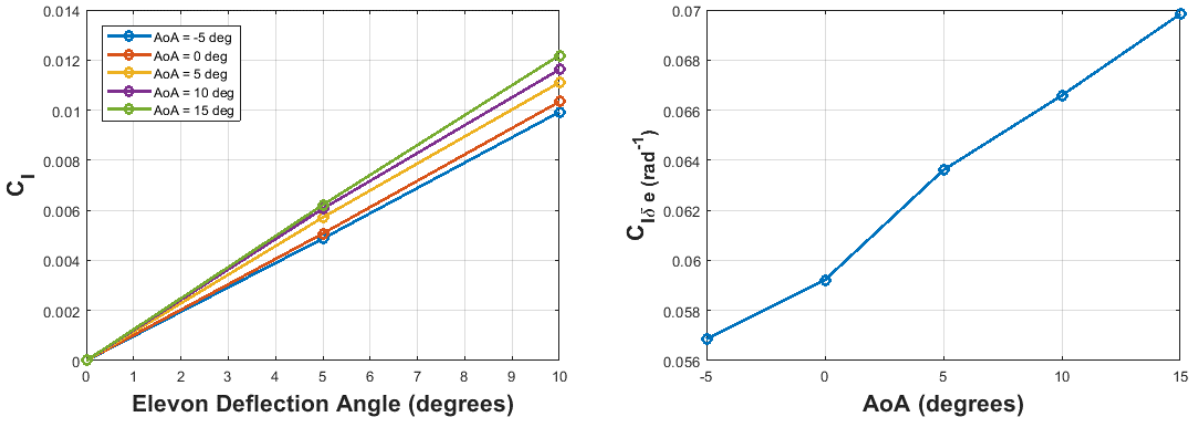

Figure 15: C_l vs elevon deflection angle (left) and $C_{l_{\delta e}}$ vs AoA (right)

Similar to Figure 14, Figure 16 presents staggered plots caused by asymmetric elevon deflections for the yaw axis, while Figure 17 illustrates elevon effectiveness with increasing AoA. Figure 17 shows that while the derivative remains positive throughout the AoA range, elevon effectiveness in yaw control reduces after an AoA of 5 degrees.

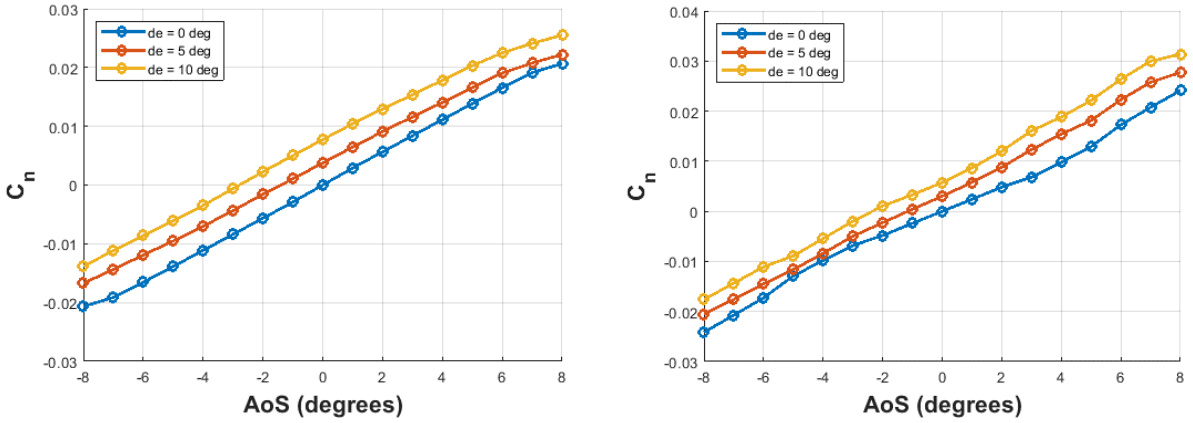

Figure 16: C_n vs AoS at -5 degrees AoA (left) and C_n vs AoS at 15 degrees AoA (right) for elevon deflection angles

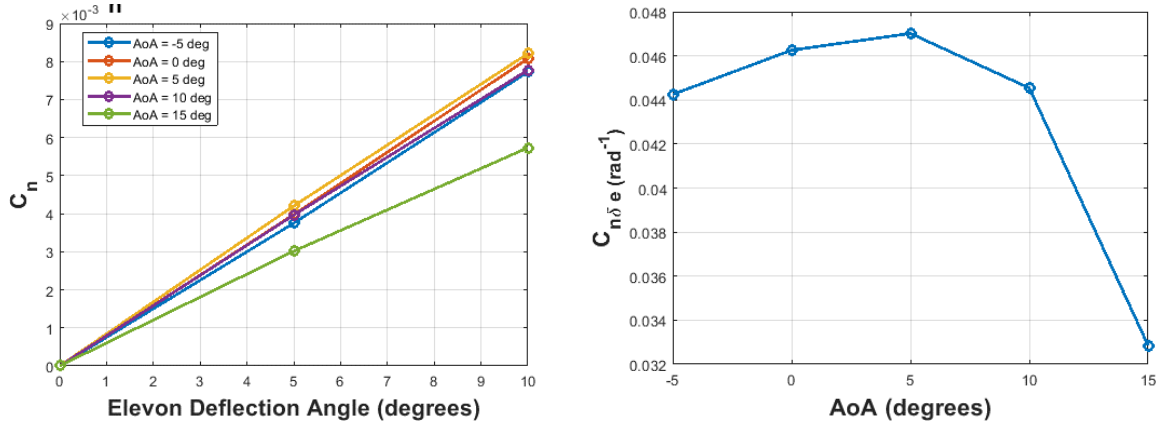

Figure 17: C_n vs elevon deflection angle (left) and $C_{n_{\delta e}}$ vs AoA (right)

Figure 18 presents the results for rolling moment coefficient for various rudder deflection angles. Note that at low AoA, the rudders appear more effective than a high AoA. This is also clearly visible in Figure 19, where the rudder control derivative for rolling moment shows decreasing values. This is potentially due to flow separation at the fin or lower flow quality at the fins due to the forebody blocking the fins from a clean flowpath.

DOI: 10.13009/EUCASS2019-128

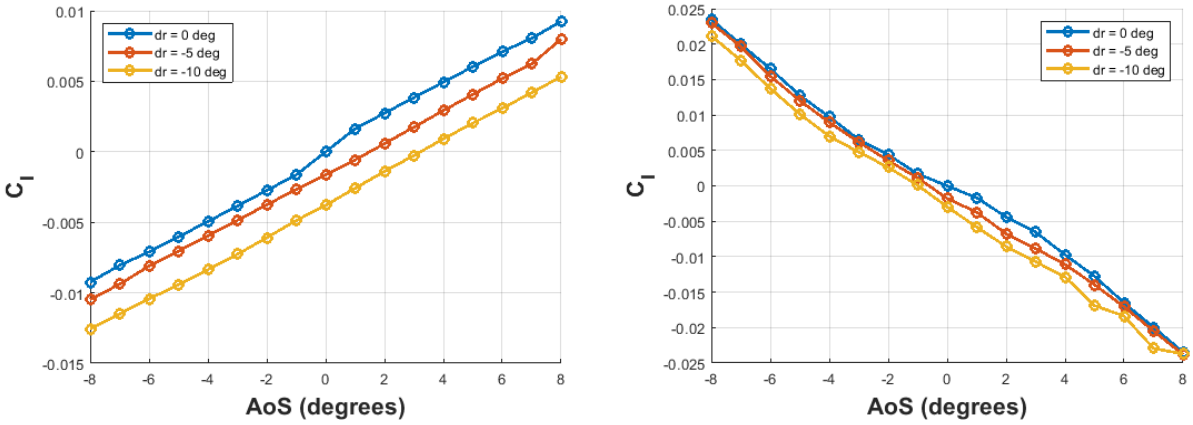

Figure 18: C_l vs AoS at -5 degrees AoA (left) and C_l vs AoS at 15 degrees AoA (right) for rudder deflection angles

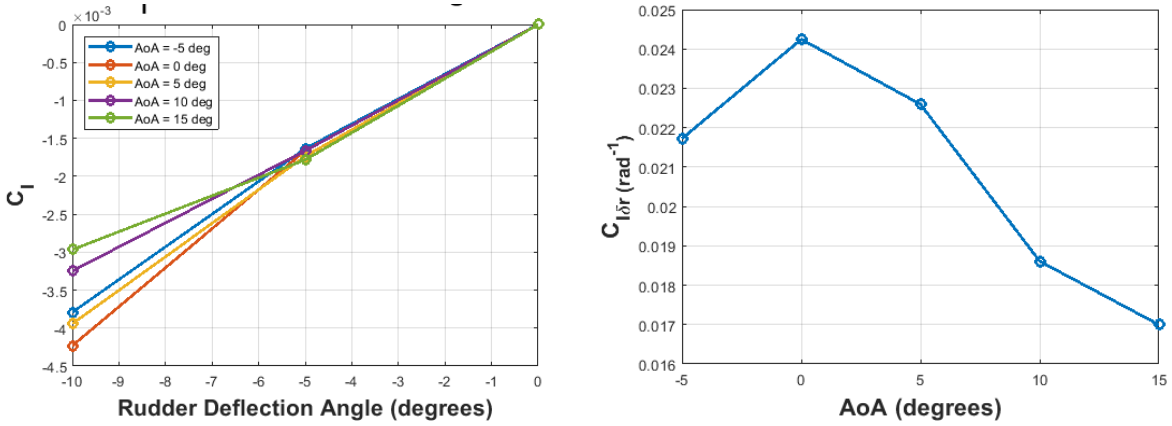

Figure 19: C_l vs elevon deflection angle (left) and $C_{l_{\delta r}}$ vs AoA (right).

Further evidence of disrupted flow to the fins is seen in Figure 20, where at high AoS and AoA, there is a sudden drop in force from the tailfins. This drop is observed at 7 degrees AoS for the -5 degree rudder deflection and at 5 degrees AoS for the -10 degree deflection. For the -5 degree AoA case, no kinks are observed, but the plots appear to narrow with increasing AoS. This is due to the cumulative effect of high rudder angle and AoS, which have an effective fin AoA approaching 20 degrees. At these angles the fin is expected to be at or approaching stall.

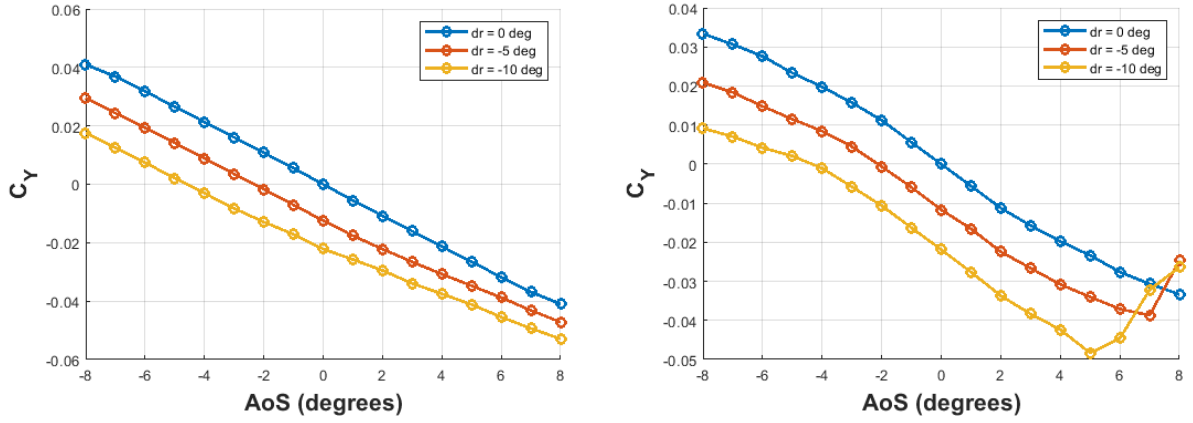

Figure 20: C_Y vs AoS at -5 degrees AoA (left) and C_Y vs AoS at 15 degrees AoA (right) for rudder deflection angles

Figure 21 presents plots of side force coefficient vs rudder deflection angle as well as the control derivative which show a maximum effectiveness at 0 deg AoA and a minimum at 10 deg AoA.

DOI: 10.13009/EUCASS2019-128

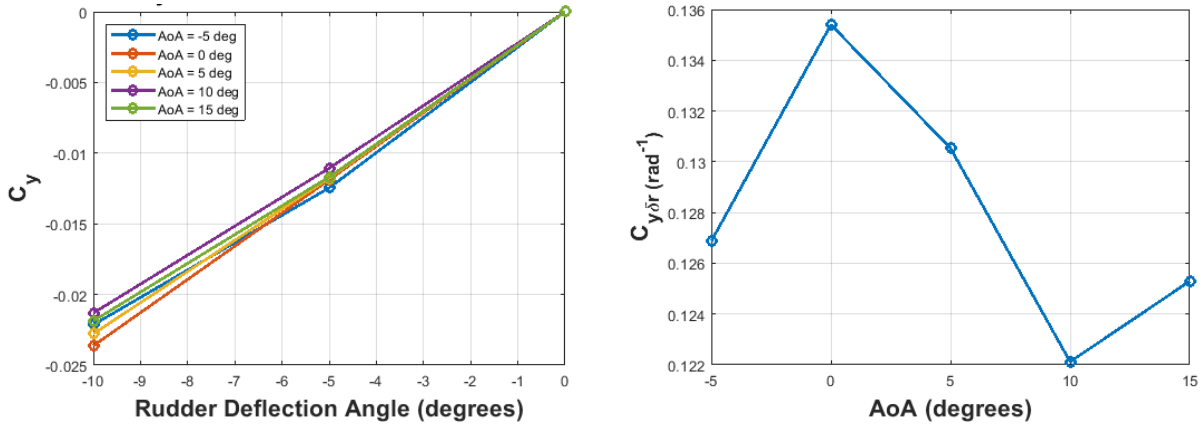

Figure 21: C_Y vs elevon deflection angle (left) and $C_{Y_{\delta r}}$ vs AoA (right)

As the side force from the fins is a major contributor to the yawing moment coefficient, the same trends from Figure 20 and Figure 21 are seen in Figure 22 and Figure 23. A reduced effectiveness in yaw from high rudder angle deflections is observed.

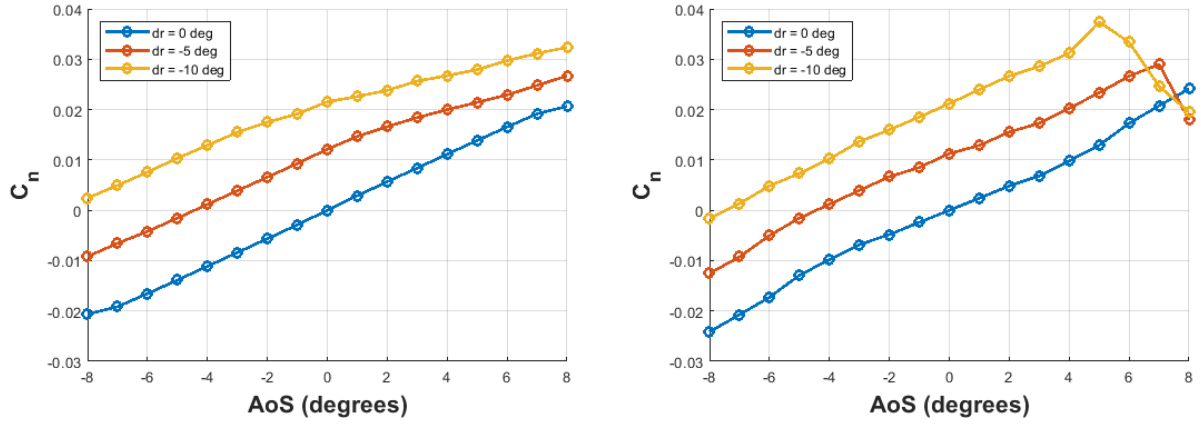

Figure 22: C_n vs AoS at -5 degrees AoA (left) and C_n vs AoS at 15 degrees AoA (right) for rudder deflection angles

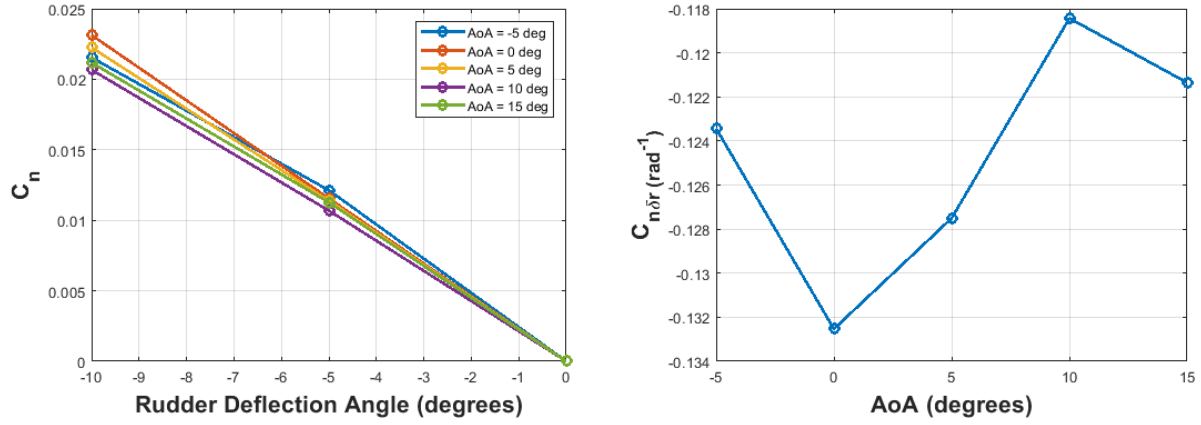

Figure 23: C_n vs elevon deflection angle (left) and $C_{n_{\delta r}}$ vs AoA (right)

Post processed images of the fins at 15 degrees AoA for -10 degrees of ruddervator deflection are illustrated in Figure 24 (-8 degrees AoS), Figure 25 (0 degrees AoS) and Figure 26 (8 degrees AoS). With increasing AoS effectively increasing the AoA of the fin, it is clear that at low AoS the vertical stabiliser has good flow quality with almost no flow separation.

DOI: 10.13009/EUCASS2019-128

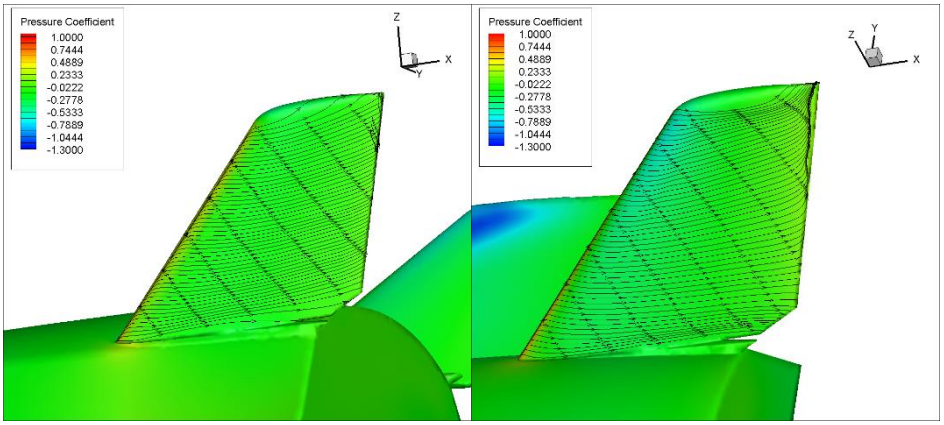

Figure 24: Leeward side of LHS fin 0 degrees AoA and -8 degrees AoS (left) and Leeward side of RHS fin 0 degrees AoA and -8 degrees AoS (right)

At 0 deg AoS, severe flow separation is observed on the right fin, but it appears to still be producing lift, as shown by the large low pressure region on the leeward side. Flow on the left-hand side remains largely attached, but evidence of secondary flow coming off the fuselage is seen.

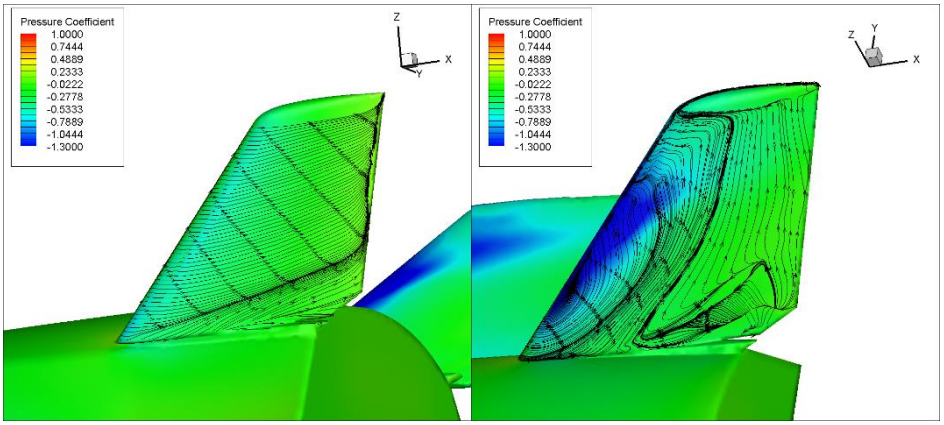

Figure 25: Leeward side of LHS fin 0 degrees AoA and -8 degrees AoS (left) and Leeward side of RHS fin 0 degrees AoA and -8 degrees AoS (right)

Complete separation and loss of suction is seen at 8 degrees AoS, which corresponds well with the loss in side force and restoring yawing moment seen in Figure 16 and 18.

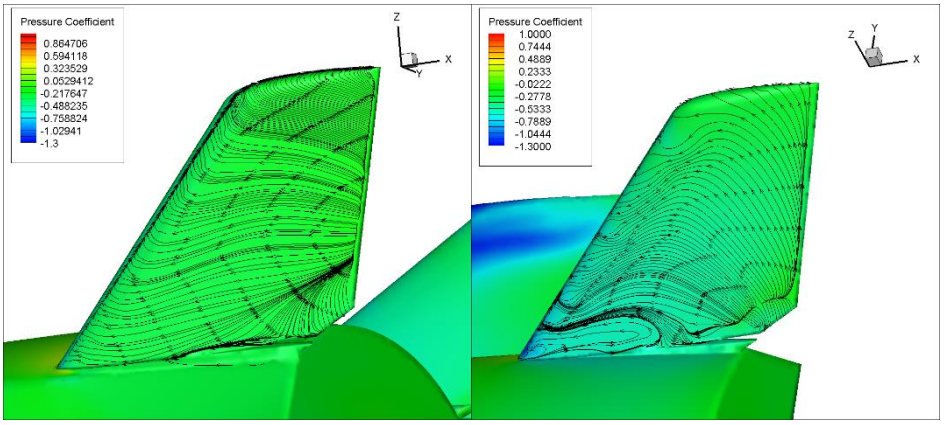

Figure 26: Leeward side of LHS fin 0 degrees AoA and -8 degrees AoS (left) and Leeward side of RHS fin 0 degrees AoA and -8 degrees AoS (right)

DOI: 10.13009/EUCASS2019-128

3.2 High Speed

Present investigations are the prosecution of what recognized by the same authors in Ref. [1], where vehicle longitudinal and lateral directional high-speed aerodynamics were investigated for clean configuration only. In this research effort, CFD investigations of concept aerodynamics, with deflected aerosurfaces with and without sideslip flow, were started. For instance, the effect of sideslip flow on vehicle lift, drag and pitching moment coefficients are summarized in Figure 27 and Figure 28. As shown, lift and drag do not change significantly while ranging from -5 to 5 deg AoS. On the other hand, the effect on pitching moment is remarkable. The same effect, but for C_Y, C_l and C_n can be found in Ref. [1], where the static stability in both longitudinal and lateral-direction flight conditions was proven.

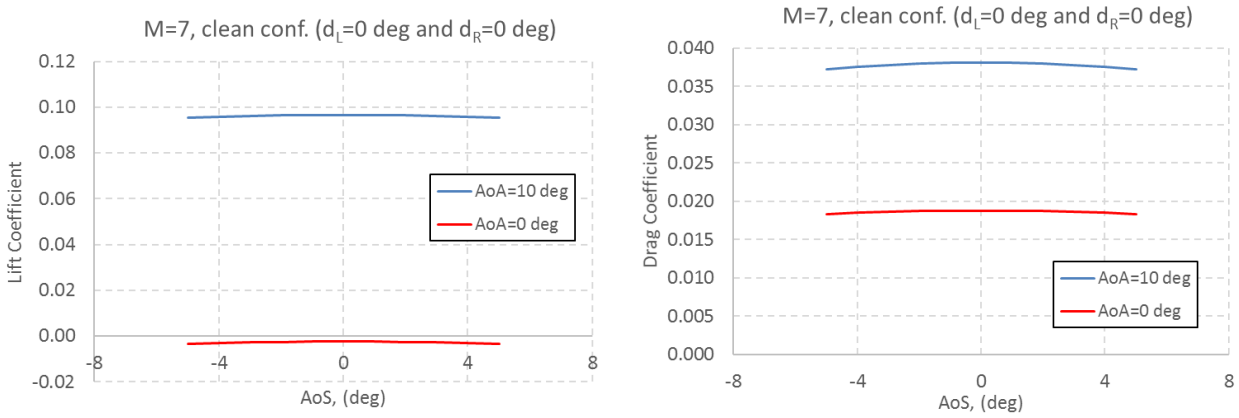

Figure 27 Lift and drag coefficients. Effect of sideslip angle on clean configuration at AoA=0 and 10 deg.

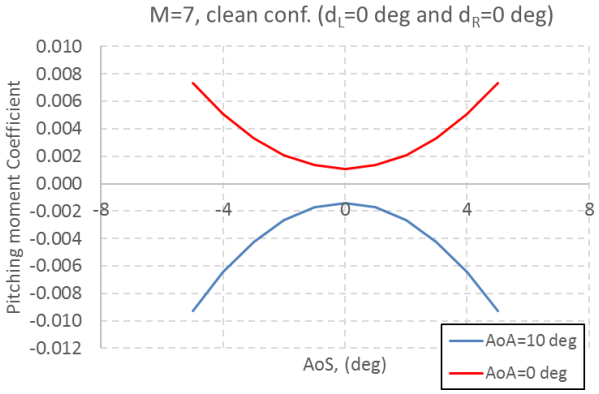

Figure 28 Pitching moment coefficient. Effect of sideslip angle on clean configuration at AoA=0 and 10. deg.

Aerodynamic control authority relies on full tail and wing flap deflections (i.e., both elevon and aileron). Therefore, the assessment of the different aileron settings is herein recognized. For instance, the effect of aileron actuation on concept's aerodynamics is summarised from Figure 29 to Figure 31.

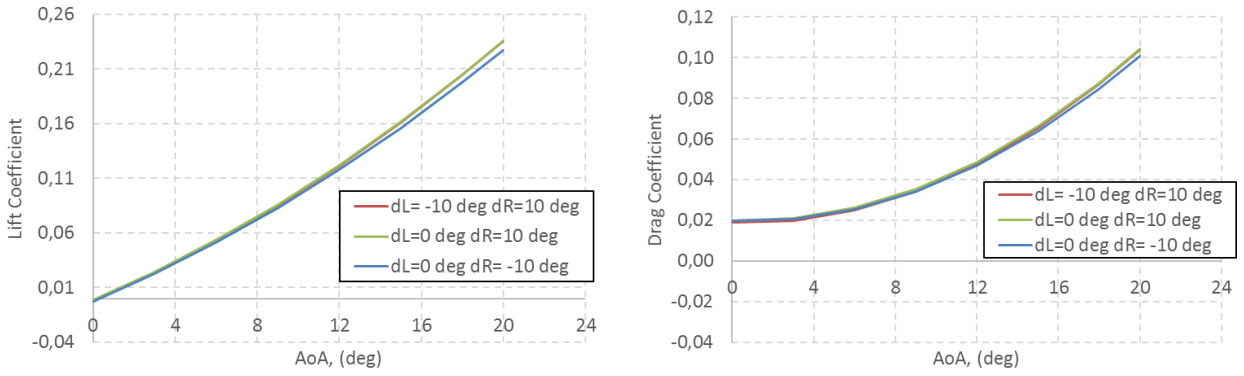

Figure 29 Lift and drag coefficients. Effect of different aileron settings.

DOI: 10.13009/EUCASS2019-128

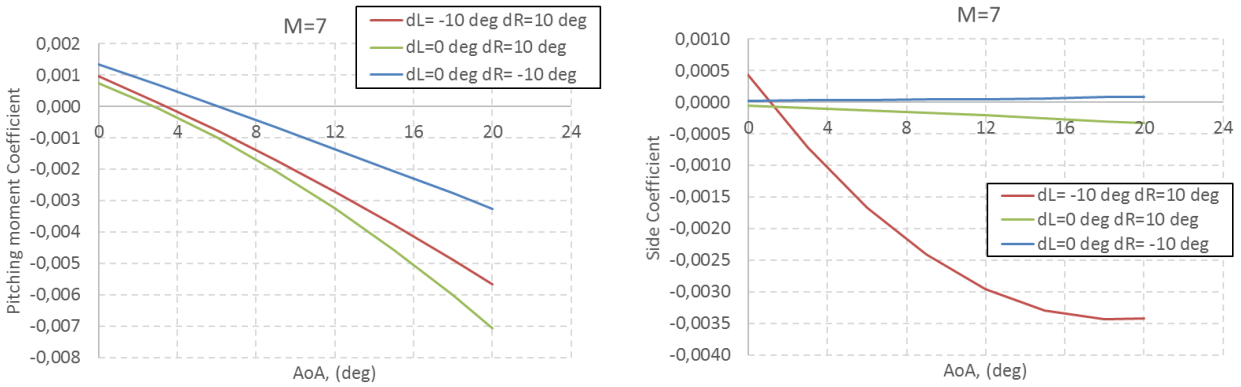

Figure 30 Pitching moment and side force coefficients. Effect of different aileron settings.

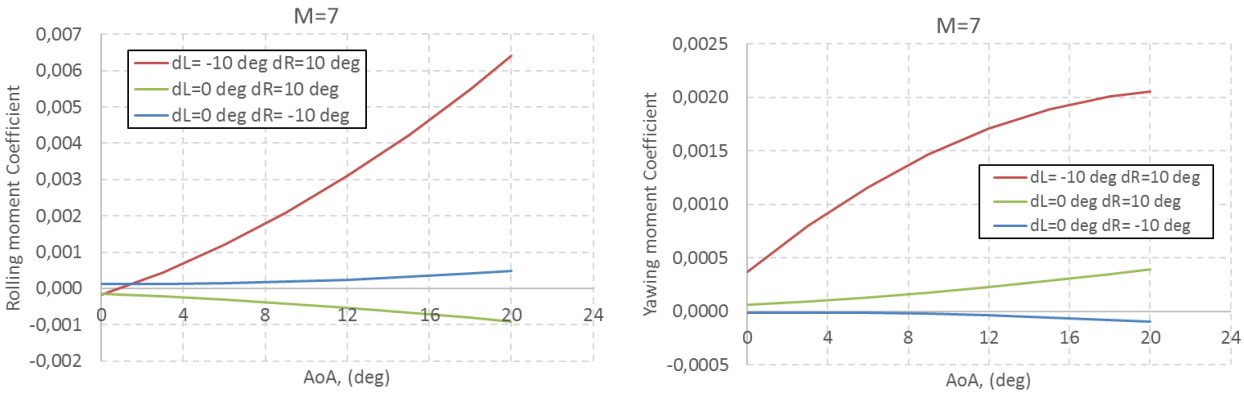

Figure 31 Rolling and Yawing moment coefficients. Effect of different aileron settings.

As shown, lift and drag are not affected by the investigated aileron setting; while the effect on the remaining force and moment coefficients appear remarkable. As far as sideslip flow contribution on flapped configuration is concerned, Figure 32 shows the pressure contours that take place on vehicle surface at AoA=10 deg, AoS=-5 deg and for aileron deflection of 10 deg (d_L=-10° and d_R=10°).

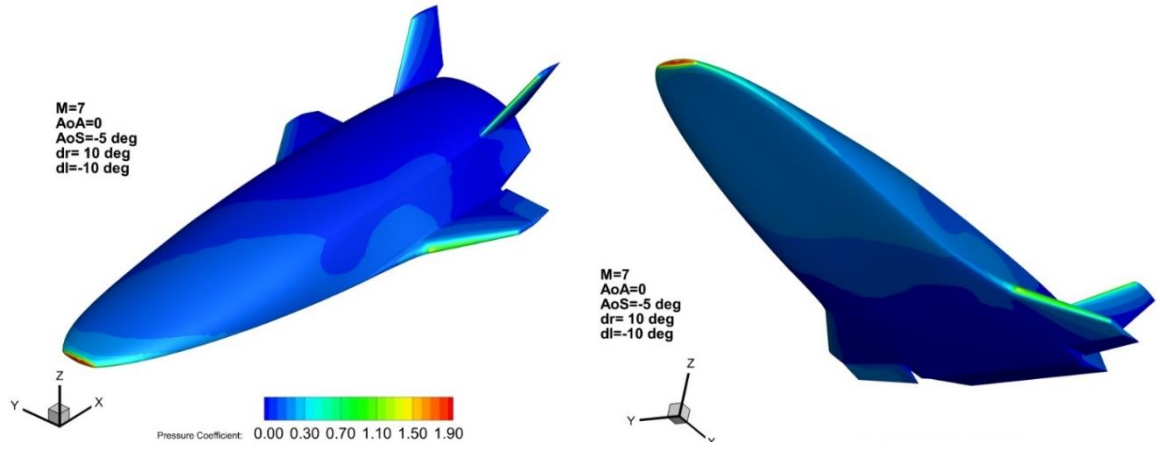

Figure 32: Pressure distribution on vehicle surface at α=0 deg, β=-5 deg with d_L= -10 deg and d_R=10 deg.

This pressure distribution, together with those coming from the effect of sideslip angles ranging from -8 to 8 deg, results in the longitudinal and lateral-directional aerodynamics summarized from Figure 33 to Figure 35. In these figures, concept aerodynamic force and moment coefficients are reported versus sideslip angle for three AoAs, namely 0, 5, and 10 deg. Figure 33 points out that lift coefficients do not significantly change while the sideslip angle is ranging from -8 to 8 deg. However, for negative AoS and AoA=0 deg, the concept features negative lift, as expected.

DOI: 10.13009/EUCASS2019-128

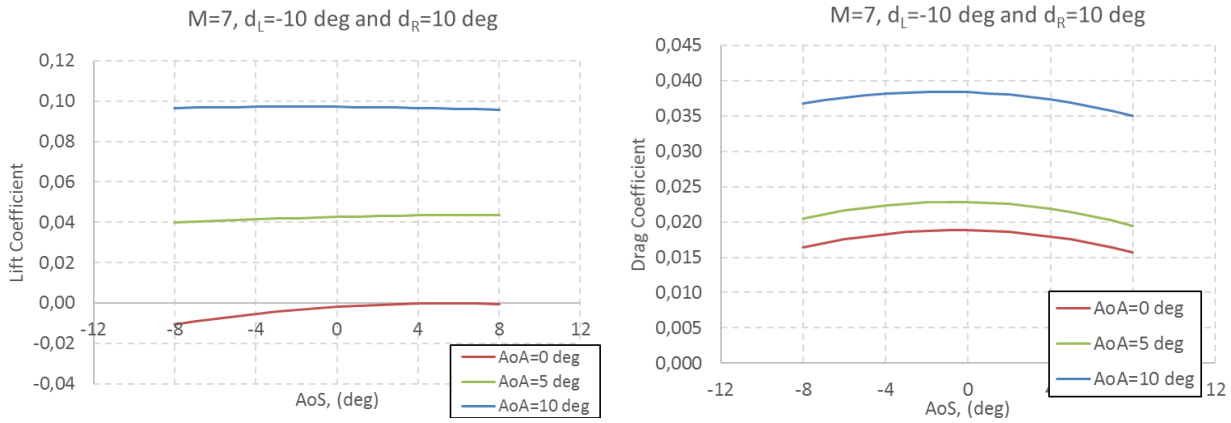

Figure 33 Lift and drag coefficients. Effect of AoS on 10 deg aileron deflections at α=0, 5 and 10 deg.

In fact, for this flow direction, only the aileron with negative deflection is working. The right aileron, even if with 10 deg deflection, is shadowed by the vehicle fuselage. On the other hand, C_D slightly decreases with AoS. Side force and pitching moment coefficients versus β are shown in Figure 34. As one can see, the vehicle aeroshape features a longitudinal trim point at about β=7 deg when the concept is flying at α=0 deg. Effects of sideslip angles on C_Y change in magnitude while α ranges from 0 to 10 deg, as expected. Indeed, as soon as vehicle attitude increases, the aileron contribution to side force decreases due to wing and fuselage shielding effects. Further, it is worth noting that sideslip derivative of side coefficient is negative, $C_{Y\beta}<0$. As known, this is one of the conditions needed to achieve lateral-directional static stability.

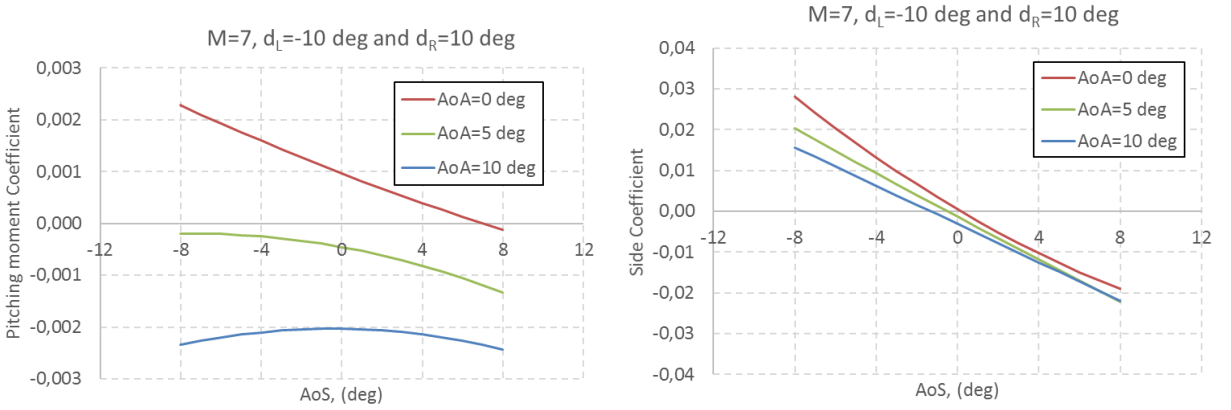

Figure 34: Effect of sideslip on 10 deg aileron deflections at AoA=0, 5 and 10 deg on C_Y and C_m.

As far as C_l and C_n are concerned, Figure 35 highlights that when the concept is at α=0 deg roll moment nulls at about β=1 deg; while yawing moment equals zero at about -4 deg, -3 deg and -1 deg AoS for 10 deg, 5 deg, and 0 deg AoA, respectively. Further, it is worth to note that above results confirm that the vehicle is statically stable in lateral-directional flight for attitude larger than 5 deg AoA.

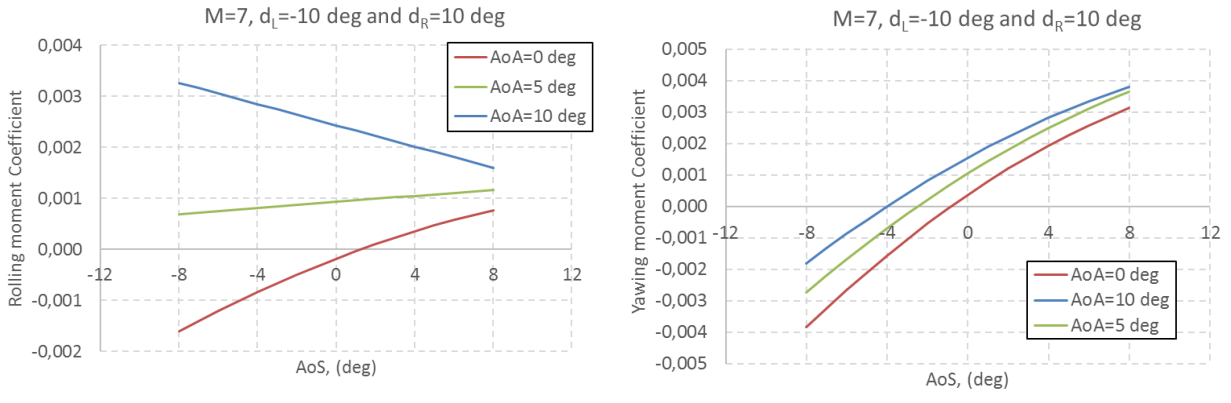

Figure 35: Effects of AoS on 10 deg aileron deflections at α=0, 5 and 10 deg on C_l and C_n.

DOI: 10.13009/EUCASS2019-128

Therefore, present aileron and vertical tails dimensions and positions seem to allow enough control authority of the vehicle concept for the given moment reference point. In fact, at these vehicle attitude, configuration and flow directions skin friction pattern highlights that the flow on left tail and wing flap is attached, as shown in Figure 36.

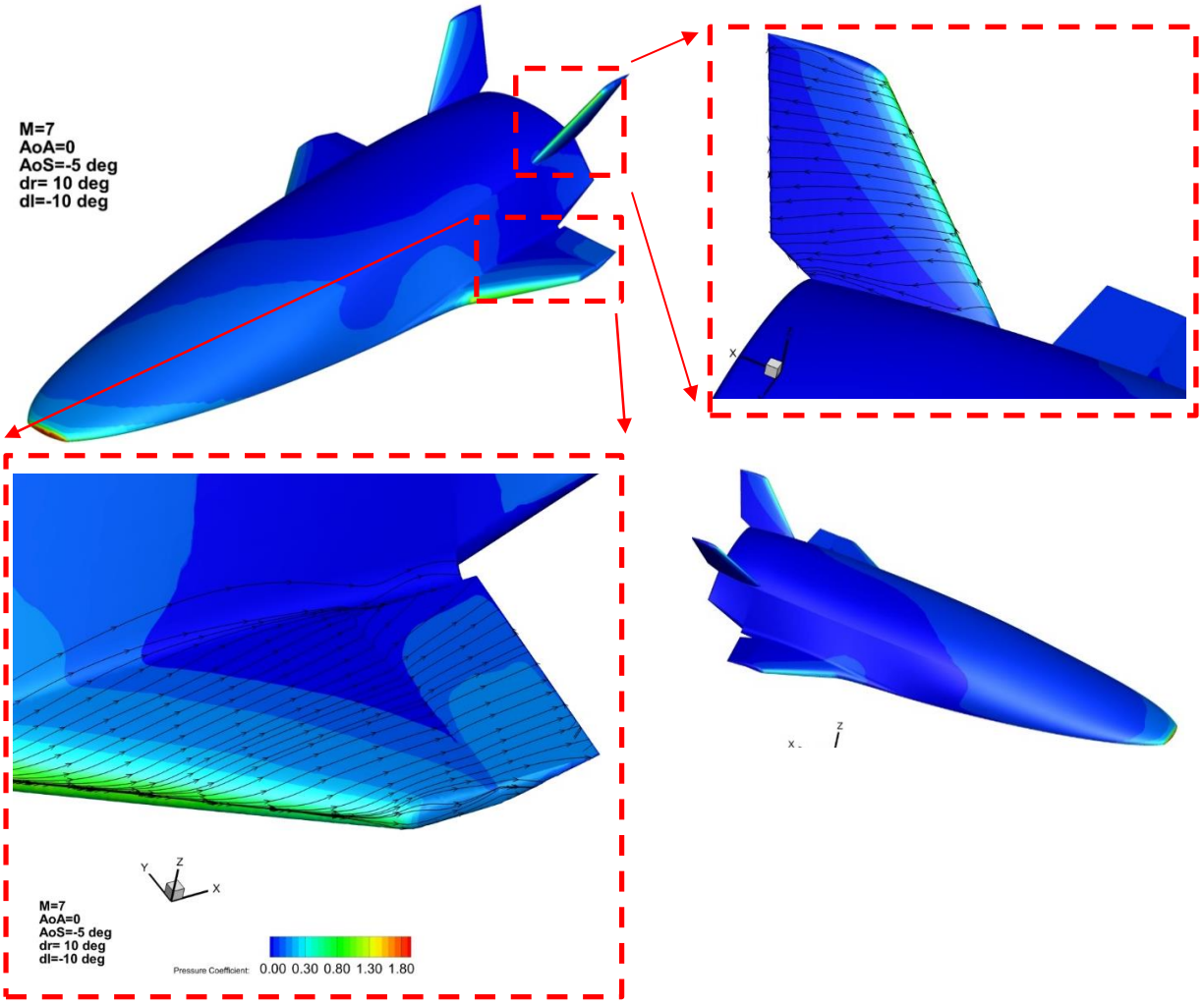

Figure 36: Effects of -5 deg AoS on 10 deg aileron deflections at α=0 deg. Skin friction lines and pressure coefficient on left wing and tail.

4. Conclusion

This paper has presented the results from lateral-directional stability and control investigations carried out on an innovative, spatuled-body aeroshape. The vehicle was analysed numerically both subsonically and at a design point of Mach 7. Low speed CFD was supported by a wind tunnel campaign, which served to validate and compare against numerical results.

Low speed wind tunnel tests showed increased stability when compared with CFD, however the vehicle was stable for almost all conditions tested. The exception was rolling moment due to sideslip, which is unstable below 0 degrees AoA based on CFD and approximately 2 degrees AoA when considering CFD. All control deflection studies showed sufficient control authority at both low and high-speed conditions. Further, subsonic results feature ranges of derivative values typical of other aircraft. Flow separation as well as disrupted flow from the fuselage around the fins was seen to have adverse effects on control effectiveness at high AoA and AoS.

Future work on this aircraft will look at further set of ruddervators and aileron deflections at high speed and at dynamic behaviour and responses to control deflections for both low and high-speed conditions.

DOI: 10.13009/EUCASS2019-128

References

[1] T. Bykerk, D. Verstraete, G. Pezzella, A. Viviani. “High and Low Speed Analysis of a Re-usable Unmanned Re-entry Vehicle”. HISST. International Conference on High-Speed Vehicle Science and Technology. Moscow. Russia. November 25-29, 2018. hisst-2018_1620897.

[2] Scigliano, R., Pezzella, G., Di Benedetto, S., Marini, M., Steelant, J., “Hexafly-Int Experimental Flight Test Vehicle (EFTV) Aero-Thermal Design”. Proceedings of the ASME 2017 International Mechanical Engineering Congress & Exposition IMECE 2017. November 3-9, 2017, Tampa, Florida, USA. ASME 2017 International Mechanical Engineering Congress and Exposition Volume 1: Advances in Aerospace Technology Tampa, Florida, USA, November 3–9, 2017.Conference Sponsors: ASME. ISBN: 978-0-7918-5834-9. Paper No. IMECE2017-70392, pp. V001T03A022; 14 pages doi:10.1115/IMECE2017-70392

[3] Roskam, J (2007). Airplane Flight Dynamics and Automatic Flight Controls (Part 1). USA: DARCorporation pp. 70-125